Nano Research 2015, 8(1): 129–139
DOI 10.1007/s12274-014-0601-1
Research Article
ISSN 1998-0124
CN 11-5974/O4

Microporous bamboo biochar for lithium–sulfur batteries

Xingxing Gu[1], Yazhou Wang[1], Chao Lai[1], Jingxia Qiu[1], Sheng Li[1], Yanglong Hou[2] (✉), Wayde Martens[3], Nasir Mahmood[2], and Shanqing Zhang[1] (✉)

[1] *Centre for Clean Environment and Energy, Environmental Futures Research Institute, Griffith School of Environment, Gold Coast Campus, Griffith University, QLD 4222, Australia*
[2] *Department of Materials Science and Engineering, College of Engineering, Peking University, Beijing 100871, China*
[3] *Science and Engineering Faculty, Queensland University of Technology QLD 4001, Australia*

Received: 7 August 2014
Revised: 7 September 2014
Accepted: 1 October 2014

KEYWORDS
biochars,
lithium-sulfur batteries,
microporous structure,
bamboo carbon–sulfur composites

ABSTRACT

Being simple, inexpensive, scalable and environmentally friendly, microporous biomass biochars have been attracting enthusiastic attention for application in lithium-sulfur (Li–S) batteries. Herein, porous bamboo biochar is activated via a KOH/annealing process that creates a microporous structure, boosts surface area and enhances electronic conductivity. The treated sample is used to encapsulate sulfur to prepare a microporous bamboo carbon–sulfur (BC-S) nanocomposite for use as the cathode for Li–S batteries for the first time. The BC-S nanocomposite with 50 wt.% sulfur content delivers a high initial capacity of 1,295 mA·h/g at a low discharge rate of 160 mA/g and high capacity retention of 550 mA·h/g after 150 cycles at a high discharge rate of 800 mA/g with excellent coulombic efficiency (⩾95%). This suggests that the BC-S nanocomposite could be a promising cathode material for Li–S batteries.

1 Introduction

Nowadays rechargeable lithium batteries (LIBs) play a predominant role in portable electronics, such as smartphones, laptops, and digital cameras and so on. However, there are still several barriers that need to be overcome to enable their applications in electric vehicles (EVs) and hybrid electric vehicles (HEVs), such as high cost, limited energy capacity and insufficient energy density. Therefore, there is increasing interest in research and development of LIBs to meet the demands of power sources for the EVs and HEVs. In comparison with traditional cathode materials, such as $LiCoO_2$ and $LiMn_2O_4$, sulfur has a high theoretical specific capacity of 1,675 mA·h/g and energy density of 2,600 Wh/kg which, as well as its high abundance, nontoxicity and inexpensiveness, make it an attractive alternative [1–3]. Therefore Li–S batteries have attracted enormous attention worldwide for the next generation of LIBs

However, it's well recognised that the commercialization of the Li–S batteries is mainly hindered by the

Address correspondence to Shangqing Zhang, s.zhang@griffith.edu.au; Yanglong Hou, hou@pku.edu.cn

low utilization and rapid capacity decay of the pure sulfur due to three factors: (1) the inherently poor electrical conductivity of sulfur (5×10^{-30} S/cm at 25 ℃) [4, 5]; (2) significant structure and volumetric changes during the charge/discharge process [6]; (3) polysulphides readily dissolve in the organic electrolyte, shuttle to the anode and then react with lithium during the charging process, resulting in deposition of insulating Li_2S_2/Li_2S at the electrode interface and causing electrical and ionic mass transfer blockages [4, 5]. Therefore, a variety of strategies including electrolyte development [7], anode modifications [8], inserting an interlayer [9], and cathode synthesis [10–12], have been intensively investigated in order to address the above issues in the charge/discharge processes. In particular, sulfur–micro/mesoporous carbon (S–MPC) composites have been regarded as one of the most promising Li–S cathodes [4–6, 10–17]. To date, although significant improvements in terms of rate capability and stability have been achieved, the aforementioned restrictions of the Li–S batteries remain unsolved as far as practical applications are concerned. The synthesis process of porous carbon materials, such as CMK-3 [10], is generally complicated and therefore costly, and lacks scalability and consistency. Thus, it is necessary to find highly efficient and low cost sources of porous carbon to build high performance sulfur-based composites.

Porous biochar, derived from biomass, has attracted increasing attention because it is inexpensive, readily available, environmentally friendly, and sustainable [4, 18]. To date various kinds of porous biochar have been reported as the sulfur host for Li–S batteries [4, 6, 19–22]. Bamboo as a natural biomass is extensively used in everyday live due to its excellent sustainability, fast growth and short maturity cycle [18]. Most importantly, bamboo has a unique well-connected three-dimensional (3D) microtexture that can be carbonized into a hierarchical porous carbonaceous structure, which possesses large surface area, high conductivity, good connectivity and a highly ordered structure [18]. Therefore, bamboo biochar is currently used as an odour absorbent and has also been used to fabricate electrodes for supercapacitors and LIBs [18, 23–26].

In this work, a commercially available and low cost bamboo biochar is used as bamboo carbon (BC). The BC sample is treated by a simple KOH/annealing strategy as shown in Scheme 1. The treated BC (T_BC) is used to synthesize microporous bamboo carbon–sulfur (T_BC-S) nanocomposites with various sulfur contents. The T_BC-S electrode shows better performance in comparison with a pristine BC-S electrode. The mechanisms responsible for the increased performances are systematically investigated using cyclic voltammetry (CV), galvanostatic charge–discharge measurements, and electrochemical impedance spectra (EIS).

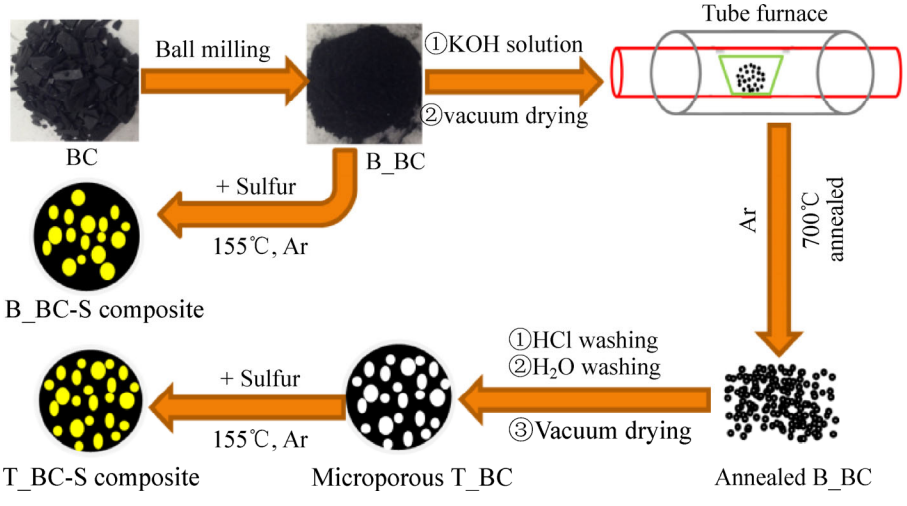

Scheme 1 The preparation process of the T_BC-S and B_BC-S composites

2 Experimental

2.1 Sample preparation

2.1.1 *Activation of BC*

Commercial bamboo carbon was first ground at 500 rpm for 3 hours with a planetary ball mill (QM-3SP04, Nanjing Nanda Instrument Plant) and sieved with a 400 mesh sieve; the resulting material is denoted ball milled bamboo carbon (B_BC). The B_BC was immersed into an 8 M KOH (analytical reagent, Sigma-Aldrich) solution for 16 h. After drying, it was annealed at 700 ˚C for 2 hours under an Ar atmosphere for activation. The resulting T_BC was collected by centrifugation, and washed with 1 M HCl solution and distilled water to remove residual KOH. The washed T_BC was then dried in a vacuum oven at 60 ˚C overnight.

2.1.2 *Synthesis of B_BC-S and T_BC-S composites*

Different amounts (i.e., 40%, 50% and 60%) of pure sulfur (analytical reagent, Sigma-Aldrich) were mixed with the B_BC and T_BC samples. These mixtures were then sealed into Teflon containers and heated at 155 ˚C for 12 hours under an Ar atmosphere. After cooling to room temperature, the B_BC-S and T_BC-S composites with different sulfur contents were obtained, and are denoted B_BC-S-50%, T_BC-S-40%, T_BC-S-50%, and T_BC-S-60%.

2.2 Sample characterization

The microstructure and morphology of all samples were examined using a JSM-7001F scanning electron microscope (SEM) (JEOL, Japan) and a Model Tecnai 20 transmission electron microscope (TEM) (FEI, USA) with an acceleration voltage of 200 kV. Energy dispersive X-ray spectroscopy (EDX) analysis and element mapping were obtained using a JSM-6610 SEM (JEOL, Japan). X-ray diffraction (XRD) patterns were obtained with a diffractometer (Model LabX-6000, Shimadzu, Japan) using Cu Kα radiation (λ = 1.54 Å) at 40 kV and 40 mA over the 2θ range of 10°–80°. The specific surface areas and pore volumes of B_BC, T_BC and T_BC-S composites were measured by the Brunauer–Emmett–Teller (BET) method using nitrogen adsorption and desorption isotherms on a Tristar 3000 system (Micromeritics, USA). Pore size distribution plot was obtained by the Horvath–Kawazoe method from the adsorption branch of the N_2 adsorption/desorption isotherms. Thermogravimetric analyses (TGA) were carried out under an N_2 atmosphere from room temperature to 600 ˚C on a Series Q500 instrument (TA Instruments, USA) to determine the sulfur loadings in the B_BC-S and T_BC-S composites. Heating rates of 10 ˚C/min were used in these TGA experiments.

2.3 Electrochemical measurements

All B_BC-S and T_BC-S samples were mixed with carbon black and polytetrafluoroethylene (PTFE, analytical reagent, Sigma-Aldrich) in a weight ratio of 70:20:10, with ethanol (analytical reagent, Sigma-Aldrich) as a dispersant. The pastes were rolled into a film with a rolling pin, and then cut into many wafers with a mould. Each wafer was approximately 0.5 cm^2 in area and had an average weight of 2 mg after dried at 60 ˚C in a vacuum oven for 12 hours. The half-cells were assembled with a home-made module in a glove box (MBRAUN, USA) with high purity argon. The configuration consists of lithium metal as the counter electrode, polypropylene (Celgard 2300) as the separator, and 1 M lithium bis(trifluoromethane) sulfonimide (LiTFSI) in 1,3 dioxolane/1,2-dimethoxyethane (DOL/ DME) (1:1, v/v) containing 0.1 M $LiNO_3$ as the electrolyte. The calculation of the specific capacity is based on the mass of the sulfur active material. The charge and discharge performances of the half-cells were tested with a LAND CT-2001A instrument (Wuhan, China), and the potential range was controlled between 1.5 and 3.0 V at room temperature. A CHI 660D electrochemical workstation (CHI Instrument, Shanghai, China) was used to perform the CV measurements with a scan rate of 0.1 mV/s and a potential from 1.5 V to 3 V. The EIS were also recorded using the same instrument over the frequency range from 100 kHz to 10 mHz.

3 Results and discussion

The thermostability of the samples was evaluated by TGA as presented in Fig. 1. It is obvious that no significant weight loss is observed for the B_BC and

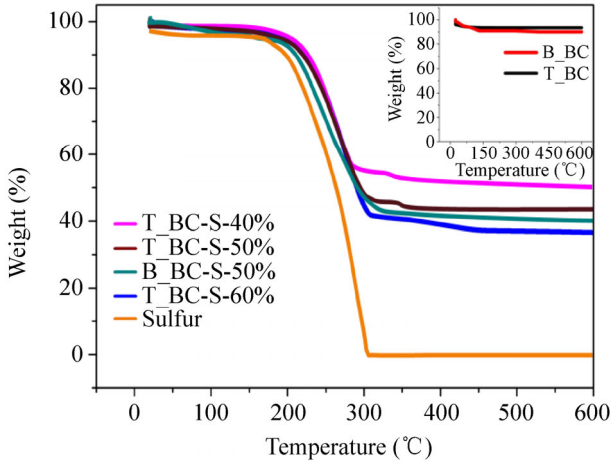

Figure 1 The TGA traces of sulfur and the B_BC, T_BC, B_BC-S and T_BC-S composites.

T_BC (inset of Fig. 1) samples between 200 ℃ and 600 ℃, which suggests that the BC samples are thermally stable in this temperature range. The element sulfur starts to vaporize at ca. 200 ℃ and this is complete at 300 ℃. Therefore, the significant weight losses of the B_BC-S and T_BC-S composites which are observed between 200 ℃ and 300 ℃ can be attributed to the evaporation of the absorbed sulfur. Accordingly, the sulfur contents in the composites are determined to be 39.5 wt.%, 50.1 wt.%, 59.7 wt.%, and 49.3 wt.% for the T_BC-S-40%, T_BC-S-50%, T_BC-S-60% and B_BC-S-50%, respectively, which are consistent with the amounts of sulfur used in their preparation processes.

As shown in Fig. 2, the T_BC shows a type I isotherm (a Langmuir type isotherm), which indicates

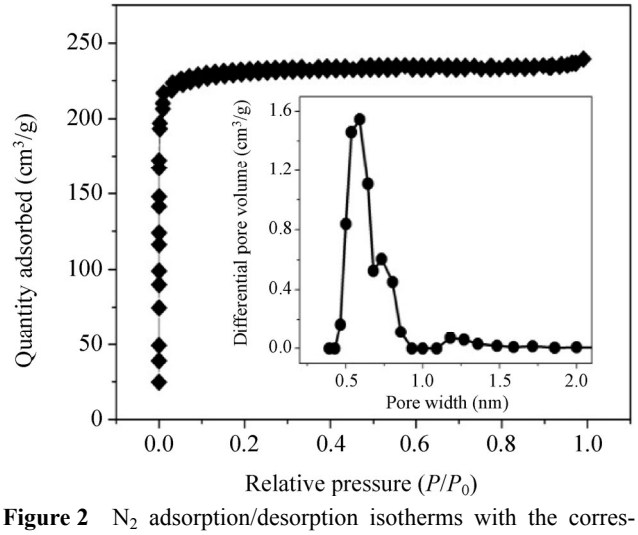

Figure 2 N_2 adsorption/desorption isotherms with the corresponding pore size distribution for T_BC.

the characteristic microporous structure of the T_BC [27]. It is worth noting that the T_BC has a narrow pore size distribution, mainly in the range ~0.6–0.75 nm as shown in the inset of Fig. 2. The values of BET surface area and pore volume of the B_BC and T_BC samples are displayed in Table 1. Interestingly, Table 1 suggests that, compared to B_BC, the specific surface area of T_BC is almost 14 times larger, while the pore volume has increased almost eightfold. This is a remarkable improvement which may be attributed to the proposed chemical process as shown in Eqs. (1)–(5) [28].

$$6KOH + 2C \rightarrow 2K + 3H_2 + 2K_2CO_3 \quad (1)$$

$$K_2CO_3 \rightarrow K_2O + CO_2 \quad (2)$$

$$CO_2 + C \rightarrow 2CO \quad (3)$$

$$K_2CO_3 + 2C \rightarrow 2K + 3CO \quad (4)$$

$$C + K_2O \rightarrow 2K + CO \quad (5)$$

It is well known that BC commonly consists of amorphous carbon and graphitic carbon [26]. After the BC is soaked in the concentrated KOH solution, KOH penetrates into entire structure of BC, including the graphitic structure, as suggested by the XRD spectrum, shown in Fig. 3. Subsequently, at high temperature (700 ℃), KOH etches the carbon framework and graphitic layer structure according to the various chemical reactions listed above. It is these reactions that are responsible for generating the porous network and opening up the layered graphitic structure [28]. This can be evidenced by the fact that the graphitic peak at a 2θ angle of 25.3° cannot be observed for the T_BC sample, as shown in Fig. 3. Instead, a new broad peak between in the 2θ range 40–50° suggests the major component of the T_BC sample is amorphous carbon [6, 19, 21].

After sulfur is loaded into the T_BC, the pore volumes and specific surface areas of the T_BC–S composite decrease sharply: for T_BC-S-50%'s specific area and

Table 1 Physical characteristic of B_BC and T_BC

Sample	BET surfacearea (m^2/g)	Total porevolume (cm^3/g)
B_BC	56.00	0.050
T_BC	791.80	0.380

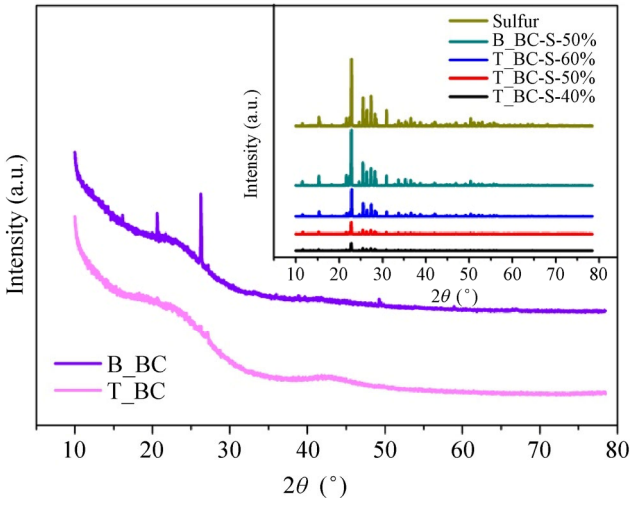

Figure 3 XRD diffractograms of sulfur and the B_BC, T_BC, B_BC-S and T_BC-S composites.

pore volume are only 0.53 m^2/g and 0.003 cm^3/g, respectively. This indicates that the elemental sulfur is embedded into the micropores of T_BC due to extremely strong physical adsorption [27, 29]. And as shown in the inset of Fig. 3, at lower sulfur loading (i.e., 40 wt.%), the weaker characteristic diffraction peaks of crystalline sulfur can be identified with low intensity, implying that most of the sulfur diffuses into the pores of the T_BC matrix, and exists in a highly dispersed or amorphous state [30]. In contrast, because the pore volume of B_BC is very small (as shown in Table 1), before the activation process the sulfur in the B_BC-S-50% composite is mainly distributed on the surface of B_BC during the heating process, leading to strong diffraction peaks of crystalline sulfur.

As shown in Figs. 4(a) and 4(b), the B_BC contains abundant pores in the range from 0.1 μm to 2 μm. The pores appear shallow as they are commonly blocked by impurities such as tar [4]. In contrast, after the material is activated, the pores in the resulting T_BC become deeper because they are unblocked. The surface of T_BC is smoother than that of B_BC, indicating the removal of the impurities. More importantly, these open macropores facilitate infiltration of the electrolyte [4]. From Fig. 4(d), the T_BC-S-50% has an obviously different morphology from those of B_BC and T_BC. After sulfur infiltration, the abundant pore structures have disappeared, and at the same time, some sulfur particle clusters on the surface of T_BC are observed, indicating that all the pores in the T_BC are saturated with sulfur and the sulfur starts to accumulate at the surface. The observation agrees well with the XRD and BET data. The EDX and elemental mapping (Fig. S1 in the Electronic Supplementary Material (ESM)) confirm that sulfur particles are distributed homogeneously in the framework of the porous T_BC.

As illustrated in Fig. 4(e), an abundant microporous structure with small pore sizes (<1 nm) of T_BC is observed in the high-resolution TEM image, which is consistent with the N_2 adsorption/desorption results. The developed microporous structure enhances both the diffusion and adsorption of the molten sulfur during the thermal treatment process, and the distribution of the electrolyte throughout the porous structure of carbon during cycling. Moreover the micropores in the T_BC act as microporous reactors and restrict the dissolution of lithium polysulfides in the organic electrolyte, due to the strong physical adsorption [27]. The high-resolution TEM image of T_BC-S-50% (Fig. 4(f)) demonstrates crystal lattice

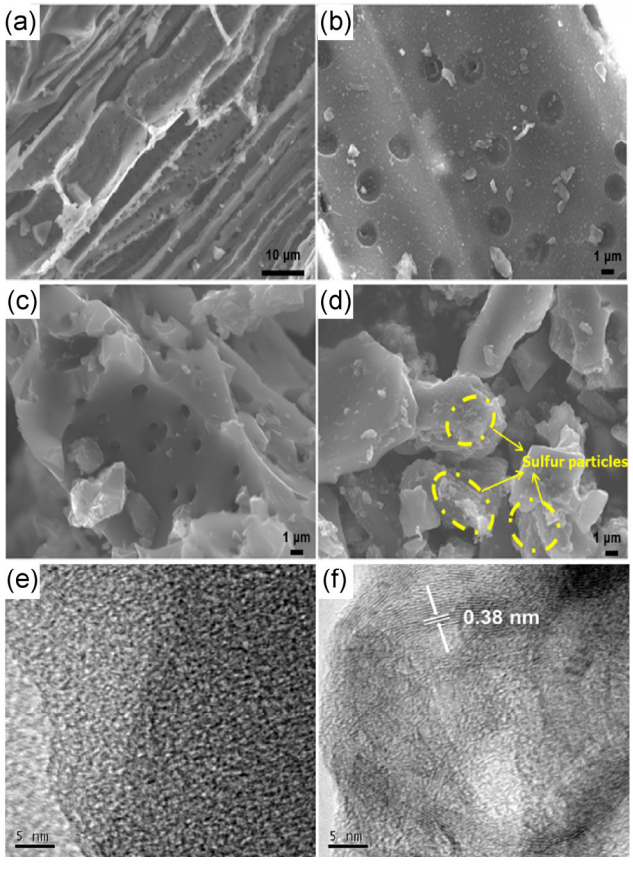

Figure 4 SEM images of B_BC (a) and (b), T_BC (c), T_BC-S-50% (d) and TEM images of the TBC (e), T_BC-S-50% (f).

fringes with a *d*-spacing of 0.38 nm, corresponding to the (222) plane of elemental sulfur. In addition, the microporous structure is scarcely visible in Fig. 4(f), again suggesting the sulfur has been fully incorporated in the micropores.

Cyclic voltammetry experiments were conducted to investigate the electrochemical mechanisms of the as-prepared Li–S batteries. Figure 5(a) shows the CV curves of the T_BC-S-50% electrode at a scan rate of 0.1 mV during the first three cycles. In the first cycle of the cathode reduction process, three peaks at approximately 2.3 V, 2.1 V, and 1.7 V are observed, which correspond to the reduction of elemental sulfur to higher-order lithium polysulphides (Li_2S_x, $4 < x < 8$) and the reduction of higher-order lithium polysulphides to lower-order lithium polysulphides, or even to insoluble Li_2S, respectively [31–33]. In the subsequent anodic scan, one asymmetric oxidation peak (which can be divided into two peaks) is observed at around 2.38 V and can be attributed to the conversion of lithium sulfides to lithium polysulfides and sulfur [31, 34]. From the second cycle onwards, the position and areas of the CV peaks remain nearly unchanged with increasing cycle number, implying good reaction reversibility and cycling stability of the nanocomposite electrode after the second cycle [31, 34, 35].

Typical voltage capacity profiles of the T_BC-S-50% at various cycles are shown in Fig. 5(b). These discharge curves show two typical plateaus (around 2.3 V and 2.1 V) like all sulfur-containing electrodes, which can be assigned to a two-step reaction of sulfur with lithium during the discharge process, agreeing well with the CV measurements [31, 32, 34]. Commonly, the long sloping plateau below 2.0 V could be only observed in the carbonate electrolyte [27, 36]. While for our results, a long sloping plateau below 2.0 V is observed in Fig. 5(b), which might result from the strong adsorption process of Li_2S_2 on the micropores in addition to the reduction process (from Li_2S_2 to Li_2S) at around 1.7 V. Similar phenomenon has been observed in the Ref. [33]. Such strong interactions should ensure the stable performance of T_BC-S-50% sample [33]. In addition, as shown in Fig. 5(b), the discharge plateaus are still obvious and stable even after 150 cycles, which confirms the excellent cycling performance (550 mAh/g after 150 cycles) of the nanocomposite cathode.

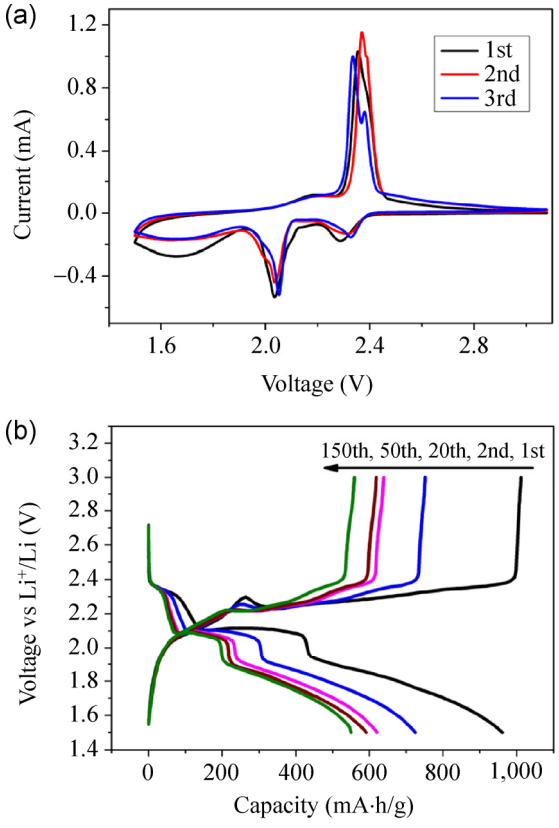

Figure 5 Cyclic voltammogram of T_BC-S-50% (a) and galvanostatic charge–discharge curves of the T_BC-S-50% cathode at 800 mA/g (b).

Figures 6(a) and 6(b) illustrates the cycling performances of B_BC-S and T_BC-S composites at rates of 160 mA/g and 800 mA/g, respectively. On the one hand, it demonstrates the cycling performance of T_BC-S-50% electrode is much better than that of B_BC-S-50% when the sulfur loading is literally the same. This can be explained as follows: (1) the T_BC material has far higher specific area and pore volume of the micropores than the B_BC material, which can provide more active sites and reduce the loss of the active material [6]; (2) the activation process removes the impurities, such as tar [4], which are detrimental to the lithium–sulfur cells; (3) the far larger number of micropores in T_BC ensure good electrical contact between sulfur and the conducting carbon framework, further facilitating Li-ion transportation by providing low resistance pathways [18, 22].

For T_BC as the conductive matrix, the initial capacity and reversible capacity first increase, and then decrease, with increasing sulfur content. For instance,

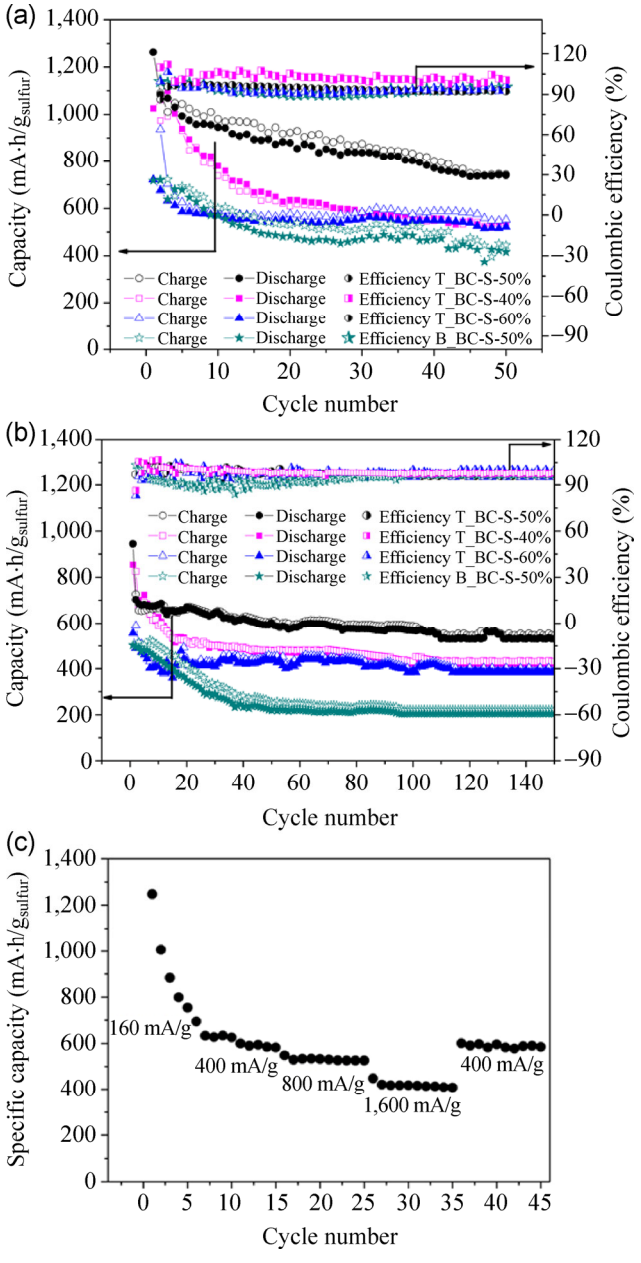

Figure 6 Cycle life of the B_BC-S and T_BC-S composites at a rate of 160 mA/g (a), and 800 mA/g (b), and the rate capability of T_BC-S-50% electrode (c).

the initial capacity first increases from 856 mA·h/g for T_BC-S-40% to 961 mA·h/g for T_BC-S-50%, and then dramatically decreases to 618 mA·h/g for T_BC-S-60% at 800 mA/g rate. After 150 cycles, the T_BC-S-50% also exhibits the highest reversible capacity of 550 mA·h/g, implying the high utilization of the active sulfur in the composite with around 50 wt.% sulfur loading [30, 37]. This clearly shows that the sulfur embedded into the bamboo carbon can directly impact the overall performance of the nanocomposite. On the one hand, if the sulfur content is too low (e.g., 40%), the polysulphides formed in the charge process can readily dissolve in the organic electrolyte solution, leading to a severe shuttle phenomenon which will cause lower sulfur utilization [37]. On the other hand, if the sulfur content is too high (e.g., 60%), insoluble Li_2S_2 or Li_2S having lower conductivity can readily be produced during the discharge process, resulting in the lower sulfur utilization percentage and rapid decline of the specific capacity [37]. Therefore, the sulfur content needs to be optimized to address the aforementioned problems. T_BC-S-50%, which contains 50% sulfur content, was found to be the best among all the tested samples.

In fact, the electrochemical performance of T_BC-S-50% is among the best reported for Li–S batteries based on other types of biochars, as shown in Table 2. In particular, the composite cathode T_BC-S-50% displays the highest initial capacity and the second highest reversible capacity (after 50 cycles). Moreover the sulfur utilization efficiency of our composite cathode is larger than for other biochar-sulfur composite cathodes.

Furthermore, an excellent rate capability performance is observed in Fig. 6(c). After the cell was activated at a 160 mA/g rate for the first five cycles, further cycling at 400 mA/g, 800 mA/g, 1,600 mA/g rates showed reversible capacities of about 600 mA·h/g, 540 mA·h/g and 410 mA·h/g, respectively. When the rate was switched to 400 mA/g again, the electrode retained its original capacity of approximately 600 mA·h/g, indicating the T_BC-S-50% cathode material is highly robust and stable [38].

Table 2 Electrochemical performance of Li–S cells basing on different porous biochar carbon

Biochar type	Initial capacity (mA·h/g)	50th cycle capacity (mA·h/g)	Rate (mA/g)	S (%)	Ref.
Pomelo peels carbon	1,280	~880	335	60	4
Pig bone carbon	1,265	643	–	–	19
Kapok carbon fibers	549	~524	670	93	21
Olive stone derived carbon	930	670	100	80	22
Bamboo carbon	1,295	756	160	50	This work

To better understand the improved electrochemical performance associated with the use of activated microporous bamboo carbon, the EIS (Fig. 7) of the as-prepared materials before discharge and after 50 cycles were measured. Before discharging, the impedance spectra are composed of a medium-to-high frequency semicircle and a long inclined line (Warburg impedance) in the low frequency region.

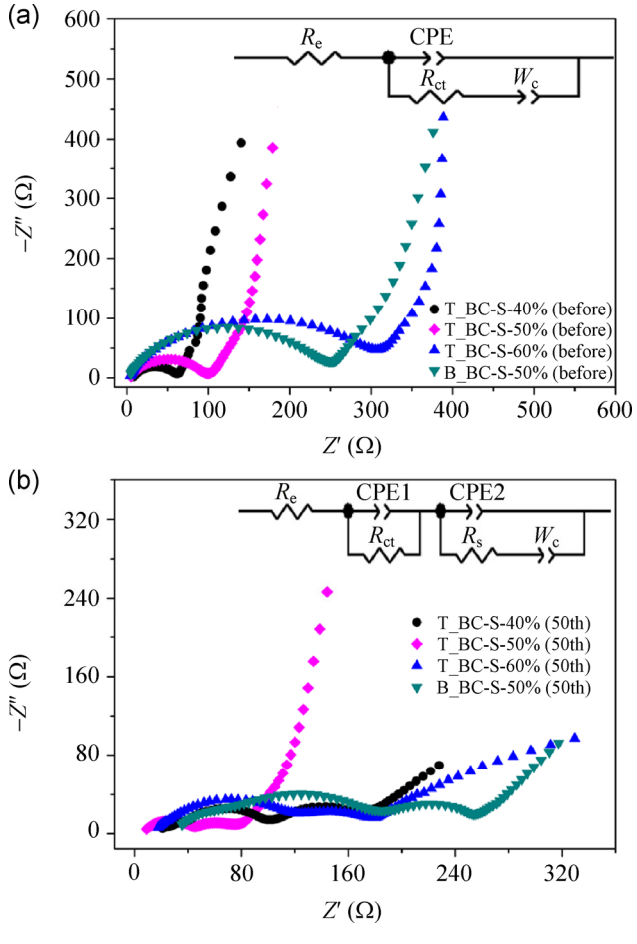

Figure 7 Nyquist plots before discharge (a) and after the 50th discharge (b) for B_BC-S and T_BC-S composites.

The semicircle is attributed to the charge transfer process at the interface between the electrolyte and sulfur electrode. The Warburg impedance is associated with semi-infinite diffusion of soluble lithium polysulfide in the electrolyte [39, 40]. After 50 cycles, the impedance spectra demonstrate two depressed semicircles followed by a short sloping line. The semicircle in the higher frequency region reflects the interfacial charge transfer process, and the semicircle in the medium frequency range is related to the solid–electrolyte-interface (SEI) film which is caused by the formation of Li_2S (or Li_2S_2) on the carbon matrix in the cathode [39, 40]. The equivalent circuit models for analysing the impedance spectra are shown in the insets of Fig. 7(a) and Fig. 7(b). R_e represents the impedance contributed by the resistance of the electrolyte, R_{ct} is the charge transfer resistance at the conductive agent interface, CPE is a constant phase element which is used instead of capacitance, R_s is the deposit diffusion resistance of SEI film, and W_c is the Warburg impedance due to the diffusion of the polysulfides within the cathode [39]. As shown in Fig. 7(a) and Table 3, the value of R_{ct} (before discharge) of T_BC-S-50% is much smaller than that of B_BC-S-50%, which can be attributed to the enhanced conductivity of the T_BC-S-50% [6, 21]. The R_{ct} values increase significantly with increasing sulfur loading (62.5, 109.3 and 310.0 Ω for the samples with 40 wt.%, 50 wt.% and 60 wt.% S content, respectively), which is mainly due to the fact that the sulfur possesses very high resistance. After 50 cycles, the R_{ct} values of all the samples decrease in comparison with that at the beginning, indicating that the irreversible deposition and aggregation of insoluble Li_2S and Li_2S_2 on the surface of the BC-S Nanocomposites, and transportation of Li-ions, becomes much easier as the cycle

Table 3 Impedance parameters simulated from the equivalent circuits

Cycle number	Resistance	T_BC-S-40%	T_BC-S-50%	T_BC-S-60%	B_BC-S-50%
Before discharge	R_e	4.5	3.6	2.2	2.4
	R_{ct}	62.5	109.3	310.0	239. 4
After 50 cycles	R_e	17.7	6.5	16.4	21.9
	R_{ct}	57.2	35.7	105.5	194.0
	R_s	42.3	39.6	49.9	57.6

number increases, which in turn leads to the high rate capability of the cathode during long cycling [35]. After 50 cycles, the R_{ct} value of T_BC-S-50% is the smallest, which may be attributed to it having highest sulfur utilization and the least pronounced shuttle phenomenon, which contribute to the T_BC-S-50% nanocomposite cathode demonstrating best performance at long cycle numbers and high charge/discharge rates [41].

4 Conclusions

Bamboo biochar has been successfully activated and used to fabricate a porous carbon–sulfur nanocomposite for use as the cathode material in Li–S batteries. This simple and facile activation process plays a key role in producing a microporous carbon with two functions: It can encapsulate sulfur and polysulphides to reduce the shuttle phenomenon during cycling and at the same time maintain electrical contact between the sulfur and the conductive carbon framework during the charge/discharge process. In addition, after the B_BC was activated, the open macropores and newly added micropores facilitate infiltration of the electrolyte into the cathode materials. Therefore, the T_BC-S samples show improved electrochemical performances compared to the B_BC-S sample. In particular, T_BC-S-50% delivers a high initial capacity of 1,262 mAh/g at a rate of 160 mA/g and a high reversible capacity of 550 mA·h/g at a rate as high as 800mA/g, with a coulombic efficiency over 95%. Consequently, the BC-S composite is a promising new cathode material for Li–S batteries.

Acknowledgements

The authors acknowledge the financial support of the ARC Discovery Grants from the Australian Research Council, the NSFC-RGC Joint Research Scheme (No. 51361165201) and NSFC (Nos. 51125001, 51172005).

Electronic Supplementary Material: Supplementary material (EDS imaging) is available in the online version of this article at http://dx.doi.org/10.1007/s12274-014-0601-1.

References

[1] Peramunage, D.; Licht, S. A solid sulfur cathode for aqueous batteries. *Science* **1993**, *261*, 1029–1032.

[2] Bruce, P. G.; Freunberger, S. A.; Hardwick, L. J.; Tarascon, J.-M. Li–O_2 and Li–S batteries with high energy storage. *Nature Mater.* **2012**, *11*, 19–29.

[3] Ji, X. L.; Nazar, L. F. Advances in Li–S batteries. *J. Mater. Chem.* **2010**, *20*, 9821–9826.

[4] Zhang, J.; Xiang, J. Y.; Dong, Z. M.; Liu, Y.; Wu, Y. S.; Xu, C. M.; Du, G. H. Biomass derived activated carbon with 3D connected architecture for rechargeable lithium−sulfur batteries. *Electrochim. Acta* **2014**, *116*, 146–151.

[5] Jayaprakash, N.; Shen, J.; Moganty, S. S.; Corona, A.; Archer, L. A. Porous hollow carbon@sulfur composites for high-power lithium–sulfur batteries. *Angew. Chem. Int. Ed.* **2011**, *50*, 5904–5908.

[6] Zhao, S. R.; Li, C. M.; Wang, W. K.; Zhang, H.; Gao, M. Y.; Xiong, X.; Wang, A. B.; Yuan, K. G.; Huang, Y. Q.; Wang, F. A novel porous nanocomposite of sulfur/carbon obtained from fish scales for lithium–sulfur batteries. *J.Mater. Chem. A* **2013**, *1*, 3334–3339.

[7] Jeddi, K.; Ghaznavi, M.; Chen, P. A novel polymer electrolyte to improve the cycle life of high performance lithium–sulfur batteries. *J. Mater. Chem. A* **2013**, *1*, 2769–2772.

[8] Lee, J.-H.; Lee, H.-Y.; Oh, S.-M.; Lee, S.-J.; Lee, K.-Y.; Lee, S.-M. Effect of carbon coating on electrochemical performance of hard carbons as anode materials for lithium-ion batteries. *J. Power Sources* **2007**, *166*, 250–254.

[9] Zhou, G. M.; Pei, S. F.; Li, L.; Wang, D. W.; Wang, S. G.; Huang, K.; Yin, L. C.; Li, F.; Cheng, H. M. A graphene–pure-sulfur sandwich structure for ultrafast, long-life lithium–sulfur batteries. *Adv. Mater.* **2014**, *26*, 625–631.

[10] Ji, X. L.; Lee, K. T.; Nazar, L. F. A highly ordered nanostructured carbon–sulfur cathode for lithium–sulfur batteries. *Nature Mater.* **2009**, *8*, 500–506.

[11] Xu, G. L.; Xu, Y. F.; Fang, J. C.; Peng, X. X.; Fu, F.; Huang, L.; Li, J. T.; Sun, S. G. Porous graphitic carbon loading ultra high sulfur as high-performance cathode of rechargeable lithium-sulfur batteries. *ACS Appl. Mater. Interfaces* **2013**, *5*, 10782–10793.

[12] He, G.; Evers, S.; Liang, X.; Cuisinier, M.; Garsuch, A.; Nazar, L. F. Tailoring porosity in carbon nanospheres for lithium–sulfur battery cathodes. *ACS Nano* **2013**, *7*, 10920–10930.

[13] Zhang, W. H.; Qiao, D.; Pan, J. X.; Cao, Y. L.; Yang, H. X.; Ai, X. P. A Li^+-conductive microporous carbon–sulfur composite for Li–S batteries. *Electrochim. Acta* **2013**, *87*, 497–502.

[14] Xi, K.; Cao, S.; Peng, X. Y.; Ducati, C.; Kumar, R. V.; Cheetham, A. K. Carbon with hierarchical pores from carbonized metal-organic frameworks for lithium sulfur batteries. *Chem. Commun.* **2013**, *49*, 2192–2194.

[15] Tao, X. Y.; Chen, X. R.; Xia, Y.; Huang, H.; Gan, Y. P.; Wu, R.; Chen, F.; Zhang, W. K. Highly mesoporous carbon foams synthesized by a facile, cost-effective and template-free Pechini method for advanced lithium–sulfur batteries. *J. Mater. Chem. A* **2013**, *1*, 3295–3301.

[16] Brun, N.; Sakaushi, K.; Yu, L. H.; Giebeler, L.; Eckert, J.; Titirici, M. M. Hydrothermal carbon-based nanostructured hollow spheres as electrode materials for high-power lithium–sulfur batteries. *Phys. Chem. Chem. Phys.* **2013**, *15*, 6080–6087.

[17] Zhang, K.; Zhao, Q.; Tao, Z. L.; Chen, J. Composite of sulfur impregnated in porous hollow carbon spheres as the cathode of Li–S batteries with high performance. *Nano Res.* **2013**, *6*, 38–46.

[18] Zhou, X. H.; Li, L. F.; Dong, S. M.; Chen, X.; Han, P. X.; Xu, H. X.; Yao, J. H.; Shang, C. Q.; Liu, Z. H.; Cui, G. L. A renewable bamboo carbon/polyaniline composite for a high-performance supercapacitor electrode material. *J. Solid State Electrochem.* **2012**, *16*, 877–882.

[19] Wei, S. C.; Zhang, H.; Huang, Y. Q.; Wang, W. K.; Xia, Y. Z.; Yu, Z. B. Pig bone derived hierarchical porous carbon and its enhanced cycling performance of lithium–sulfur batteries. *Energy Environ. Sci.* **2011**, *4*, 736–740.

[20] Chung, S. H.; Manthiram, A. A natural carbonized leaf as polysulfide diffusion inhibitor for high-performance lithium–sulfur battery cells. *ChemSusChem* **2014**, *7*, 1655–1661.

[21] Tao, X. Y.; Zhang, J. T.; Xia, Y.; Huang, H.; Du, J.; Xiao, H.; Zhang, W. K.; Gan, Y. P. Bio-inspired fabrication of carbon nanotiles for high performance cathode of Li–S batteries. *J. Mater. Chem. A* **2014**, *2*, 2290–2296.

[22] Moreno, N.; Caballero, A.; Hernán, L.; Morales, J. Lithium–sulfur batteries with activated carbons derived from olive stones. *Carbon* **2014**, *70*, 241–248.

[23] Tan, Z. Q.; Sun, L. S.; Xiang, J.; Zeng, H. C.; Liu, Z. H.; Hu, S.; Qiu, J. R. Gas-phase elemental mercury removal by novel carbon-based sorbents. *Carbon* **2012**, *50*, 362–371.

[24] Kannan, N.; Sundaram, M. M. Kinetics and mechanism of removal of methylene blue by adsorption on various carbons—A comparative study. *Dyes Pigm.* **2001**, *51*, 25–40.

[25] Kim, Y. J.; Lee, B. J.; Suezaki, H.; Chino, T.; Abe, Y.; Yanagiura, T.; Park, K. C.; Endo, M. Preparation and characterization of bamboo-based activated carbons as electrode materials for electric double layer capacitors. *Carbon* **2006**, *44*, 1592–1595.

[26] Jiang, J.; Zhu, J. H.; Ai, W.; Fan, Z. X.; Shen, X. N.; Zou, C. J.; Liu, J. P.; Zhang, H.; Yu, T. Evolution of disposable bamboo chopsticks into uniform carbon fibers: A smart strategy to fabricate sustainable anodes for Li-ion batteries. *Energy Environ. Sci.* **2014**, *7*, 2670–2679.

[27] Zhang, B.; Qin, X.; Li, G. R.; Gao, X. P. Enhancement of long stability of sulfur cathode by encapsulating sulfur into micropores of carbon spheres. *Energy Environ. Sci.* **2010**, *3*, 1531–1537.

[28] Wang, J. C.; Kaskel, S. KOH activation of carbon-based materials for energy storage. *J. Mater. Chem.* **2012**, *22*, 23710–23725.

[29] Shinkarev, V. V.; Fenelonov, V. B.; Kuvshinov, G. G. Sulfur distribution on the surface of mesoporous nanofibrous carbon. *Carbon* **2003**, *41*, 295–302.

[30] Zhang, Y. Z.; Liu, S.; Li, G. C.; Li, G. R.; Gao, X. P. Sulfur/polyacrylonitrile/carbon multi-composites as cathode materials for lithium/sulfur battery in the concentrated electrolyte. *J. Mater. Chem. A* **2014**, *2*, 4652–4659.

[31] Zhou, G. M.; Yin, L. C.; Wang, D. W.; Li, L.; Pei, S. F.; Gentle, I. R.; Li, F.; Cheng, H. M. Fibrous hybrid of graphene and sulfur nanocrystals for high-performance lithium–sulfur batteries. *ACS Nano* **2013**, *7*, 5367–5375.

[32] Li, D.; Han, F.; Wang, S.; Cheng, F.; Sun, Q.; Li, W. C. High sulfur loading cathodes fabricated using peapodlike, large pore volume mesoporous carbon for lithium–sulfur battery. *ACS Appl. Mater. Interfaces* **2013**, *5*, 2208–2213.

[33] Li, Z.; Jiang, Y.; Yuan, L. X.; Yi, Z. Q.; Wu, C.; Liu, Y.; Strasser, P.; Huang, Y. H. A highly ordered meso@microporous carbon-supported sulfur@smaller sulfur core–shell structured cathode for Li–S batteries. *ACS Nano* **2014**, *8*, 9295–9303.

[34] Huang, J. Q.; Liu, X. F.; Zhang, Q.; Chen, C. M.; Zhao, M. Q.; Zhang, S. M.; Zhu, W. C.; Qian, W. Z.; Wei, F. Entrapment of sulfur in hierarchical porous graphene for lithium–sulfur batteries with high rate performance from −40 to 60 °C. *Nano Energy* **2013**, *2*, 314–321.

[35] Ding, B.; Yuan, C. Z.; Shen, L. F.; Xu, G. Y.; Nie, P.; Zhang, X. G. Encapsulating sulfur into hierarchically ordered porous carbon as a high-performance cathode for lithium–sulfur batteries. *Chem. —Eur. J.* **2013**, *19*, 1013–1019.

[36] Zhang, S. S. Sulfurized carbon: A class of cathode materials for high performance lithium/sulfur batteries. *Front. Energy Res.* **2013**, *1*, 1–9.

[37] Wang, Y. X.; Huang, L.; Sun, L. C.; Xie, S. Y.; Xu, G. L.; Chen, S. R.; Xu, Y. F.; Li, J. T.; Chou, S. L.; Dou, S. X.; et al. Facile synthesis of a interleaved expanded graphite-embedded sulfur nanocomposite as cathode of Li–S batteries

with excellent lithium storage performance. *J. Mater. Chem.* **2012**, *22*, 4744–4750.

[38] Seh, Z. W.; Li, W. Y.; Cha, J. J.; Zheng, G. Y.; Yang, Y.; McDowell, M. T.; Hsu, P. C.; Cui, Y. Sulfur–TiO_2 yolk–shell nanoarchitecture with internal void space for long-cycle lithium–sulfur batteries. *Nature Commun.* **2013**, *4*, 1331–1336.

[39] Wang, W. G.; Wang, X.; Tian, L. Y.; Wang, Y. L.; Ye, S. H. *In situ* sulfur deposition route to obtain sulfur–carbon composite cathodes for lithium–sulfur batteries. *J. Mater. Chem. A* **2014**, *2*, 4316–4323.

[40] Ahn, W.; Kim, K.-B.; Jung, K.-N.; Shin, K.-H.; Jin, C.-S. Synthesis and electrochemical properties of a sulfur-multi walled carbon nanotubes composite as a cathode material for lithium sulfur batteries. *J. Power Sources* **2012**, *202*, 394–399.

[41] Choi, H. S.; Oh, J. Y.; Park, C. R. One step synthesis of sulfur–carbon nanosheet hybrids via a solid solvothermal reaction for lithium sulfur batteries. *RSC Adv.* **2014**, *4*, 3684–3690.